

| | | | |
|-----------------------------|---|-----------------|---|
| $X_{T_i}, Y_{T_i}, Z_{T_i}$ | elastic force in the i^{th} segment of a rope element in the inertial body reference frame | X_A, Y_A, Z_A | components of artificial force in an inertial reference frame |
| L_B, M_B, N_B | total applied moments on a body about its mass center expressed in the body reference frame | L_A, M_A, N_A | components of artificial moment applied to a body about its mass center expressed in the body reference frame |
| f_{TV}, f_{RV} | artificial force and moment factors proportional to translational velocity and rotational velocity | | |

INTRODUCTION

Removal of overburden in surface mining operations is effectively accomplished by dragline excavation systems. A typical dragline excavation system is shown in Figures 1 and 2. An open bucket and rigging components are supported from above by a cable routed over a long boom which extends above the mine. Overburden is removed by dragging the bucket along the ground by a cable, and dumping it elsewhere. The bucket is indirectly controlled by an operator in the excavator through rotation of the boom about a vertical axis and payout and windup of the hoist and drag ropes.

For slowly operating dragline excavation systems, static system models provide a satisfactory estimate of loads that is utilized in structural sizing of components. Static system models also provide bucket position and orientation information for various hoist and drag rope lengths and

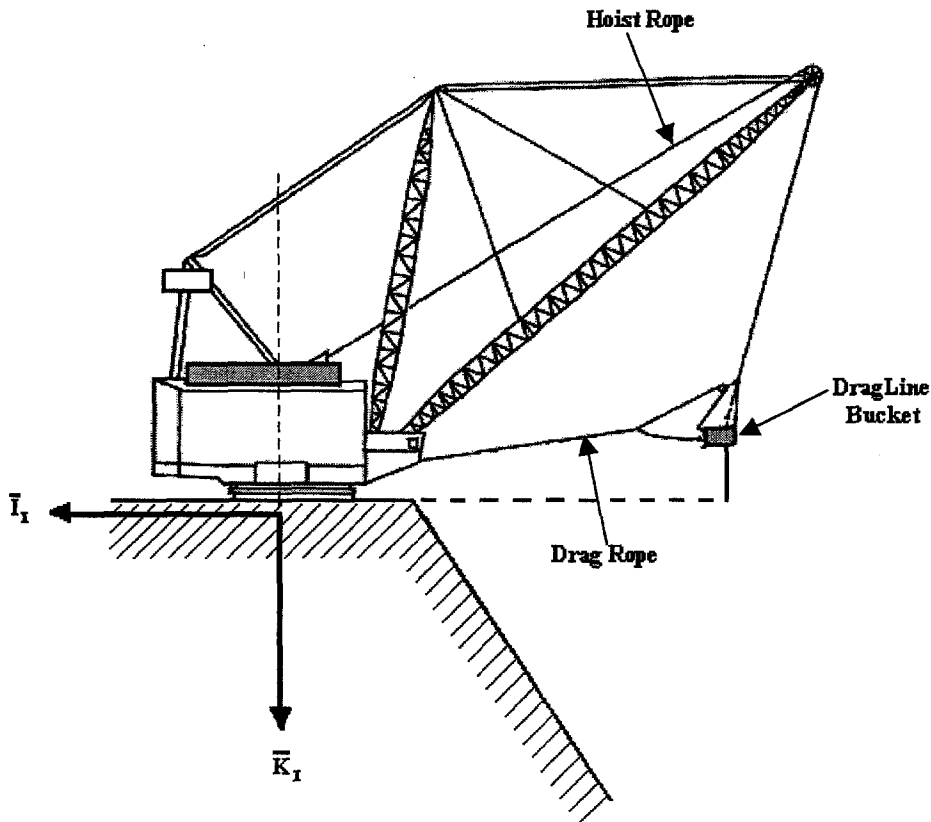


Figure 1. Dragline excavation system schematic.

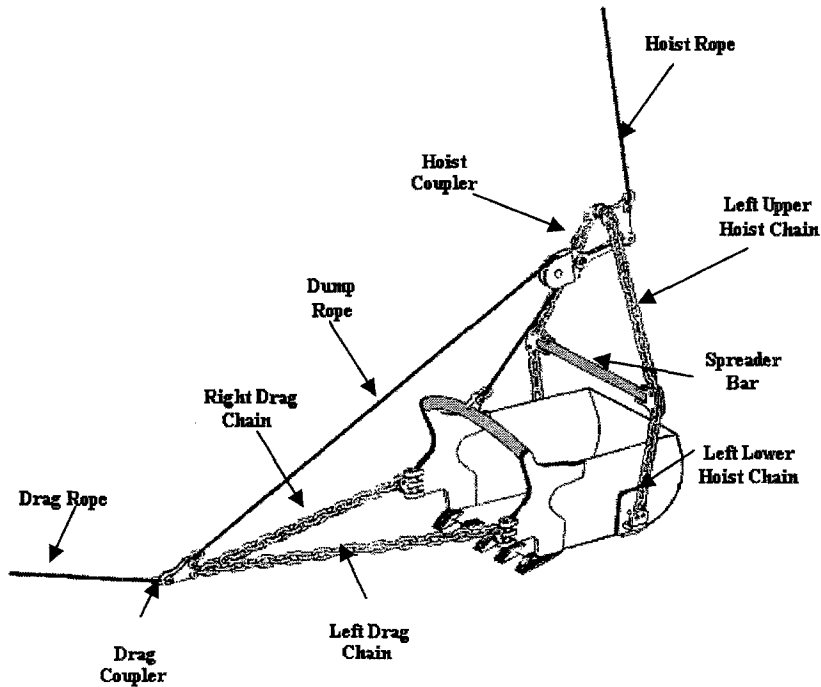


Figure 2. Dragline bucket schematic.

various bucket riggings that is useful for site excavation planning. In cases where relatively rapid maneuvering of the dragline system is encountered, the use of a dynamic dragline excavation model is more appropriate for estimating bucket orientation excursions and maximum loads on different components. Since both static and dynamic models of a dragline excavation system prove helpful in the design and analysis of these systems, a comprehensive method capable of performing both types of analysis is desirable.

Several research groups have developed dragline excavation system models at various levels of sophistication for different analytical purposes. McCoy and Crowgey [1] investigated static and dynamic dragline bucket tightline control. Using simple geometric analysis, they constructed both static and dynamic tightline limits based on the length of the drag and hoist ropes and subsequently used these limits as part of an antitightline control system. Haneman, Hayes and Lumley [2] reported on dragline performance evaluations using physical modeling. Rigging geometry and bucket size were optimized using physical modeling and compared against field data. Pathak, Dasgupta and Chattopadhyay [3] generated a method to compute the working zone of a dragline bucket. A graphical approach for determination of the bucket path profile of a standard dragline was indicated, considering a three period duty cycle in each operation. Hainsworth, Corke and Winstanley [4] used machine vision techniques to remotely measure the location of a dragline bucket in space. Using only a single camera, an image segmentation process is used to classify the bucket and to identify its position in the scene. Ridley and Corke [5] developed a technique to estimate dragline bucket pose under gravity loading. Their model is based on static equilibrium of the loads on the different components of the system.

Given a complex dynamic model of a dragline excavation system, static pose conditions can be computed by setting all derivatives of the state vector to zero and subsequently solving the remaining nonlinear algebraic equations for the static conditions. A host of numerical methods are available for this purpose [6]. In theory, a dynamic model of a dragline excavation system can be used to perform both static and dynamic analysis where static analysis is performed by integrating the dynamic equations of motion to a steady state with the hoist and drag rope lengths held constant. This basic approach is computationally expensive due to the complex

nature of dragline excavation systems and the associated long simulation run time required for the system to reach a steady-state condition. In this paper, a technique is presented that greatly accelerates convergence to steady state by adding artificial forces and moments to each body in the system that are proportional to the velocity of the body. In steady state, the artificial forces are zero and the achieved steady-state condition is the steady-state condition for the dragline excavation system. The artificial forces and moments are designed to rapidly damp motion of the excavator system. To illustrate the benefits of this approach, an example 1/16th scale dragline excavation system is considered using a complex dragline excavation system dynamic model. The model includes rigid fully three-dimensional motion of the bucket, spreader bar, drag cluster, and hoist cluster as well as three-dimensional motion of flexible chains and ropes. Simulation results are compared with data measured from a 1/16th scale dragline excavator model.

DYNAMIC MODEL OF A DRAGLINE EXCAVATION SYSTEM

The dynamic event considered here consists of the motion of a complete dragline excavation system. As shown in Figures 1 and 2, the total system contains four rigid bodies and nine ropes. The rigid bodies include the bucket, drag cluster, hoist cluster, and spreader bar. The ropes include the drag rope, dump rope, hoist rope, left drag chain, left lower hoist chain, left upper hoist chain, right drag chain, right lower hoist chain, and right upper hoist chain. The surface of the ground is assumed to be a satisfactory inertial reference. As shown in Figure 1, the inertial reference frame is a right-handed coordinate system defined with its origin on the ground surface located below the excavator at the point of azimuth rotation of the excavator. The \vec{I}_I and \vec{J}_I axes form the ground plane while the \vec{K}_I axis completes the right-handed triad and points into the ground.

Each rope segment is dynamically modeled as a set of particles connected by a standard linear solid visco-elastic element. All the mass elements of the system including all bodies (bucket, drag cluster, hoist cluster, spreader bar) and all particles on each rope segment (left lower hoist chain, right lower hoist chain, left upper hoist chain, right upper hoist chain, left drag chain, right drag chain, dump rope, drag rope, hoist rope) are connected to other system mass elements by elastic elements. Consequently, each body can be considered individually. Connection forces are simply treated as external forces acting on each body. Thus, derivatives of the state vector can be directly computed from the state vector in a straight forward manner.

Generic Rope Segment Equations of Motion

The dynamic equations for all rope segments assume the same structural form. Figure 3a depicts a typical rope segment consisting of a single length of rope with both ends attached to a moving body. Figure 3b provides a schematic on how the flexible rope element is discretized for dynamic modeling purposes. Each rope segment is split into n_r particles and $n_r + 1$ elastic elements using truss finite elements. A standard linear solid visco-elastic element is used to connect particles. Collectively, the motion of the particles defines the motion of the complete rope segment. Each particle on a rope segment is a point mass possessing three translation degrees of freedom. Forces that drive the motion of the particles include particle weight and adjacent elastic element line forces. The dynamic equations for one particle on a rope segment are structurally the same for all particles, so the formulas to follow are shown only for the i^{th} particle on an arbitrary rope segment

$$\begin{Bmatrix} \dot{x}_{R_i} \\ \dot{y}_{R_i} \\ \dot{z}_{R_i} \end{Bmatrix} = \begin{Bmatrix} u_{R_i} \\ v_{R_i} \\ w_{R_i} \end{Bmatrix}, \quad (1)$$

$$\begin{Bmatrix} \dot{u}_{R_i} \\ \dot{v}_{R_i} \\ \dot{w}_{R_i} \end{Bmatrix} = \frac{1}{m_{R_i}} \begin{Bmatrix} X_{T_i} - X_{T_{i+1}} \\ Y_{T_i} - Y_{T_{i+1}} \\ Z_{T_i} - Z_{T_{i+1}} \end{Bmatrix} + \begin{Bmatrix} 0 \\ 0 \\ g \end{Bmatrix} + \frac{1}{m_{R_i}} \begin{Bmatrix} X_{A_i} \\ Y_{A_i} \\ Z_{A_i} \end{Bmatrix}. \quad (2)$$

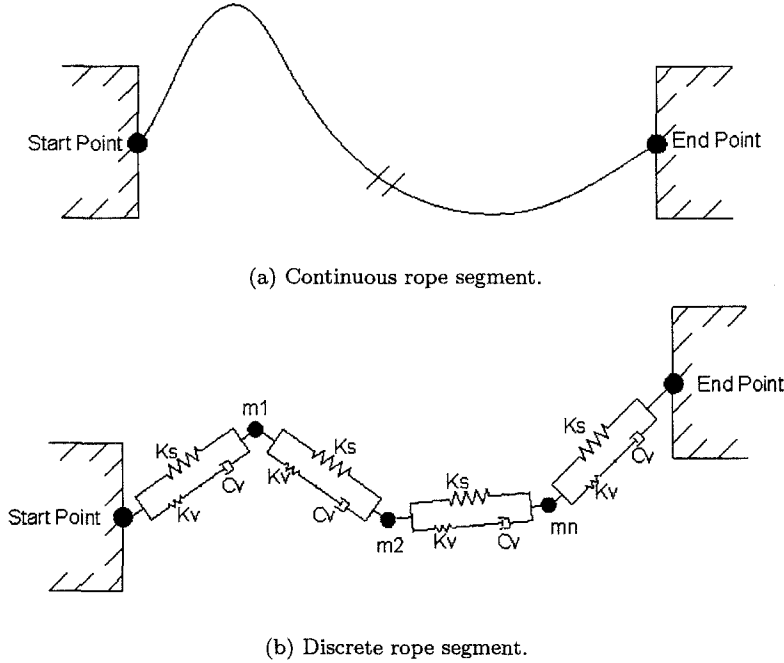


Figure 3. Rope dynamic model schematic.

In equation (2), m_{R_i} is the mass of the i^{th} particle on a rope segment and g is the gravitational constant. Terms $X_{T_i}, Y_{T_i}, Z_{T_i}$ and $X_{T_{i+1}}, Y_{T_{i+1}}, Z_{T_{i+1}}$ represent the line force vector components expressed in the inertial reference frame of the line elements adjacent to the i^{th} particle while terms $X_{A_i}, Y_{A_i}, Z_{A_i}$ represent an artificial force used to rapidly settle bead vibration.

The line forces are caused by strain of the rope and are directed parallel to the line. Rope line flexibility generates resistive stiffness and damping forces proportional to rope line segment extension and extension rate.

Equations (3) and (4) provide expressions for the line tension force, F_{R_i} , in terms of the strain and strain rate of the elastic line element

$$\dot{F}_{R_i} + \frac{K_{vR_i}}{C_{vR_i}} F_{R_i} = \begin{cases} (K_{vR_i} + K_{sR_i})\dot{s}_{R_i} + \frac{K_{vR_i}K_{sR_i}}{C_{vR_i}} s_{R_i}, & s_{R_i} - L_{R_i} > 0, \\ 0, & s_{R_i} - L_{R_i} \leq 0, \end{cases} \quad (3)$$

$$s_{R_i} = \sqrt{\Delta x_{R_i}^2 + \Delta y_{R_i}^2 + \Delta z_{R_i}^2}. \quad (4)$$

In equation (3), K_{R_i} and C_{R_i} are the stiffness and damping coefficients for an individual elastic line element. Also, L_{R_i} is the nominal unstretched line length of an individual line element. The first condition in equation (3) represents the normal tension condition between two adjacent particles. In this case, the distance between the two adjacent particles is greater than the unstretched elastic line element length and a nonzero tension force in the line persists. The second condition in equation (3) is the slack condition. It stipulates that when the unstretched elastic line element length is greater than the distance between two adjacent particles, the tension force decays to zero.

Using rope segment position difference and velocity difference vectors, an expression for the elastic line force can be directly formed

$$\begin{Bmatrix} X_{R_i} \\ Y_{R_i} \\ Z_{R_i} \end{Bmatrix} = \frac{F_{R_i}}{\sqrt{\Delta x_{R_i}^2 + \Delta y_{R_i}^2 + \Delta z_{R_i}^2}} \begin{Bmatrix} \Delta x_{R_i} \\ \Delta y_{R_i} \\ \Delta z_{R_i} \end{Bmatrix}. \quad (5)$$

The number of state variables required to model a rope segment can be large. Consider a rope segment split into 20 particles. Since each particle requires six state variables and each segment

requires an additional state variable for the line force, this rope segment would require a total of 141 state variables to define the motion of the complete rope segment.

Generic Body Equations of Motion

The dynamic equations for all body elements assume the same structural form. This section develops the basic dynamic equations of motion used for any body element. Each body is modeled as rigid and undergoes three-dimensional motion. Hence, 12 state variables are required to describe the motion of each rigid body at a given instant in time. The degrees of freedom for each body include three position components of the mass center of the body as well as three Euler orientation angles of the body. The translational dynamics of the mass center of an arbitrary body are given by equations (6) and (7)

$$\begin{Bmatrix} \dot{x}_B \\ \dot{y}_B \\ \dot{z}_B \end{Bmatrix} = \begin{Bmatrix} u_B \\ v_B \\ w_B \end{Bmatrix}, \quad (6)$$

$$\begin{Bmatrix} \dot{u}_B \\ \dot{v}_B \\ \dot{w}_B \end{Bmatrix} = \begin{Bmatrix} \frac{X_B}{m_B} \\ \frac{Y_B}{m_B} \\ \frac{Z_B}{m_B} + g \end{Bmatrix}. \quad (7)$$

In equation (7), m_B is the mass of the body and X_B, Y_B, Z_B are the components of the external rope coupling forces on the body expressed in the inertial reference frame.

The orientation of a body element is defined by a sequence of three body fixed Euler angle rotations [7]. Starting from the inertial reference frame a rotation of θ_B is executed about the \vec{J}_I axis. The resulting rotated reference frame is called the O frame. Next, the O frame is rotated about the \vec{I}_O axis by angle ϕ_B . The resulting reference frame is denoted the T frame. The T frame is subsequently rotated about the \vec{K}_T axis by angle ψ_B yielding the body reference frame. Angles ϕ_B, θ_B , and ψ_B are the Euler angles associated with the body. The kinematic relationship between time derivatives of the Euler angles and body frame angular velocity components is shown in equation (8)

$$\begin{Bmatrix} \dot{\phi}_B \\ \dot{\theta}_B \\ \dot{\psi}_B \end{Bmatrix} = \begin{bmatrix} c\psi_B & -s\psi_B & 0 \\ s\psi_B & c\psi_B & 0 \\ c\phi_B & c\phi_B & 1 \\ s\psi_B t\phi_B & c\psi_B t\phi_B & 1 \end{bmatrix} \begin{Bmatrix} p_B \\ q_B \\ r_B \end{Bmatrix}. \quad (8)$$

Equation (8) uses the following shorthand notation for trigonometric sine, cosine, and tangent functions: $s_\alpha \equiv \sin \alpha$, $c_\alpha \equiv \cos \alpha$, $t_\alpha \equiv \tan \alpha$. The rotational dynamic equation for a body is given in equation (9)

$$\begin{Bmatrix} \dot{p}_B \\ \dot{q}_B \\ \dot{r}_B \end{Bmatrix} = [I_B]^{-1} \left[\begin{Bmatrix} L_B \\ M_B \\ N_B \end{Bmatrix} - \begin{bmatrix} 0 & -r_B & q_B \\ r_B & 0 & -p_B \\ -q_B & p_B & 0 \end{bmatrix} [I_B] \begin{Bmatrix} p_B \\ q_B \\ r_B \end{Bmatrix} \right]. \quad (9)$$

In equation (9), I_B denotes the mass moment of inertia matrix of the body about its own mass center and L_B, M_B, N_B represent the components of the total externally applied moment vector on the body about its own mass center expressed in its own reference frame.

Rope Edge Point Position and Velocity

Edge point position and velocity of a rope segment is required for visco-elastic line force computation. For edge points of a rope segment that are fixed on a body of the system, expressions

for the position and velocity are formed from the motion of the connection point on the body. The inertial position vector components of the connection of a rope segment and a body is constructed as the distance from the inertial reference frame to the mass center of the body plus the distance vector from the body mass center to the connection point

$$\begin{Bmatrix} x_C \\ y_C \\ z_C \end{Bmatrix} = \begin{Bmatrix} x_B \\ y_B \\ z_B \end{Bmatrix} + [T_{B \rightarrow I}] \begin{Bmatrix} SL_C^B - SL_B \\ BL_C^B - BL_B \\ WL_C^B - WL_B \end{Bmatrix}. \quad (10)$$

Components x_C, y_C, z_C in equation (10) represent the inertial position components of a rope segment and body interface. The inertial location of the mass center of the body is denoted as x_B, y_B, z_B . The second term in equation (10) is the inertial position vector components of the distance from the mass center of the body to the interface point. Matrix $T_{B \rightarrow I}$ is an orthonormal transformation relating the body reference frame to the inertial reference frame

$$T_{B \rightarrow I} = \begin{bmatrix} c_{\psi_B} c_{\theta_B} + s_{\psi_B} s_{\phi_B} s_{\theta_B} & -s_{\psi_B} c_{\theta_B} + c_{\psi_B} s_{\phi_B} s_{\theta_B} & c_{\phi_B} s_{\theta_B} \\ s_{\psi_B} c_{\phi_B} & c_{\psi_B} c_{\phi_B} & -s_{\phi_B} \\ -c_{\psi_B} s_{\theta_B} + s_{\psi_B} s_{\phi_B} c_{\theta_B} & s_{\psi_B} s_{\theta_B} + c_{\psi_B} s_{\phi_B} c_{\theta_B} & c_{\phi_B} c_{\theta_B} \end{bmatrix}. \quad (11)$$

Components SL_C^B, BL_C^B, WL_C^B are the body frame coordinates of the interface point while the components SL_B, BL_B, WL_B are the body frame coordinates of the body mass center. The velocity of the interface point with respect to inertial space is obtained by differentiating equation (10).

Some rope segment edge points are not connected to bodies included in the dynamic system. For example, the end point of the hoist rope is connected to the hoist reel. For end points not attached to a body element of the system, the motion of the connection point is known as a function of time. Prior specification of an excavation maneuver defines the inertial position and velocity of the hoist reel, drag reel, and boom points. Furthermore, definition of an excavator maneuver also yields the length of line of the hoist and drag reels as a function of time. Computationally, any prescribed motion variables are determined by linear interpolation of a table of data with time as the abscissa and the prescribed motion parameter as the ordinate.

Body Forces and Moments

The forces and moments acting on a body of the dragline excavation system consist of body weight and elastic line forces from rope segments connected to the body. Each rope segment is divided into n_r particles and $n_r + 1$ adjoining elastic elements. The visco-elastic forces applied to a body are generated from either the first or last element, depending on whether the connection is a beginning or ending connection point for the rope segment. Beginning connections use the first line element force of a rope segment while ending connections use the last line element force of a rope segment

$$\begin{Bmatrix} X_B \\ Y_B \\ Z_B \end{Bmatrix} = \sum_{j=1}^{n_c} a_j \begin{Bmatrix} X_{T_{e_j}} \\ Y_{T_{e_j}} \\ Z_{T_{e_j}} \end{Bmatrix}. \quad (12)$$

In equation (12), the index e_j is either 1 or $n_r + 1$ depending on whether the j^{th} rope segment connection is a beginning or ending connection. When the connection is a beginning connection $a_j = -1$ and when the connection is an ending connection $a_j = 1$. The moment about the mass center of a body due to the connection forces shown above is computed as a cross product of the distance vector from the mass center to the connection location and the connection force. Both the distance vector and the connection forces are expressed in the body reference frame so the resulting moments are also expressed in the body reference frame as required in the equations of motion

$$\begin{Bmatrix} L_B \\ M_B \\ N_B \end{Bmatrix} = \sum_{j=1}^c a_j [S_{C_j}] [T_{B \rightarrow I}]^T \begin{Bmatrix} X_{T_{e_j}} \\ Y_{T_{e_j}} \\ Z_{T_{e_j}} \end{Bmatrix}. \quad (13)$$

In equation (13), S_{C_j} is a matrix cross product operator.

ARTIFICIAL FORCES AND MOMENTS

In the equations of motion described above, the bead dynamic equations and the body translational dynamic equations contain an artificial force term while the body rotational dynamic equations contain an artificial moment term. These artificial forces and moment are loads that do not actually exist in the system being modeled but are added to the equations of motion to accelerate convergence of the system to a steady state. To obtain an equilibrium condition, the equations of motion are integrated forward in time until a steady-state condition is achieved. Since the interest in this effort is focused on the equilibrium condition, and not the specific path toward equilibrium, application of artificial forces and moments does not alter the equilibrium state provided the artificial forces and moments are zero at the equilibrium point. Artificial forces proportional to velocity equal zero when the system is quiescent and, thus, provide a functional form from which artificial loads can be generated.

The artificial velocity force is based on the concept of fluid dynamic damping, which produces forces and moments that are proportional to the square of velocity and are in the direction opposite of motion. For a bead,

$$\begin{Bmatrix} X_{A_i} \\ Y_{A_i} \\ Z_{A_i} \end{Bmatrix} = -\frac{f_T f_{TV}}{V_{R_i}} \begin{Bmatrix} u_{R_i} \\ v_{R_i} \\ w_{R_i} \end{Bmatrix}. \quad (14)$$

The formula for a body takes on the same structure, except the components of the mass center velocity of the body are used rather than bead velocity components. Function f_{TV} depends on the total velocity $V_{R_i} = \sqrt{u_{R_i}^2 + v_{R_i}^2 + w_{R_i}^2}$ and is proportional to the mass of the body with upper and lower limits applied. The artificial velocity moment depends on the angular velocity

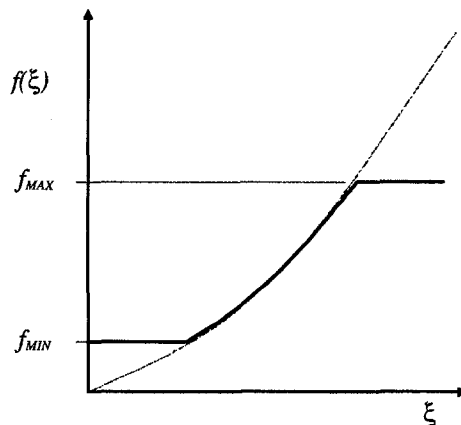


Figure 4. Functional form of artificial force and moment factors (f_{TV} and f_{RV}).

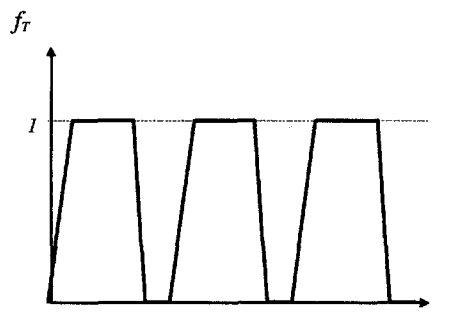


Figure 5. Functional form of artificial force and moment time factor (f_T).

components of a body and are directed opposite to the direction of motion

$$\begin{Bmatrix} L_A \\ M_A \\ N_A \end{Bmatrix} = -\frac{f_T f_{RV}}{\Omega_B} \begin{Bmatrix} p_B \\ q_B \\ r_B \end{Bmatrix}. \quad (15)$$

Function f_{RV} depends on the total angular velocity $\Omega_B = \sqrt{p_B^2 + q_B^2 + r_B^2}$ and is proportional to the average of the diagonal elements of the inertia matrix of the body with upper and lower limits applied. Figure 4 presents a diagram of the basic functional form of all artificial force and moment factors. The artificial force and moment factors f_{TV} and f_{RV} are selected to minimize the simulation time required to reach steady state. The translational artificial force factor f_T is used to smoothly blend the artificial force and moment terms into the simulation. It is equal to 1 when the artificial force and moment factors are active and equal to 0 when the artificial force and moment terms are inactive. Figure 5 shows an example of the artificial force and moment time factor, f_T .

DETERMINATION OF EQUILIBRIUM STATES FOR DRAGLINE EXCAVATION SYSTEM

Using a standard fourth-order Runge-Kutta method, an equilibrium state is determined by integrating the dynamic equations forward in time from an initial state until the system settles, such that the velocity of all components is sufficiently small. When the numerical integration process begins from a nonequilibrium state or when the hoist or drag rope length is changed, the system first vibrates and subsequently settles to an equilibrium position. The equilibrium state of the dragline excavation system for different operational hoist and drag rope lengths is determined by intermittently reeling in or paying out the hoist and/or drag rope. After the hoist or drag ropes are reeled in or payed out, the ropes are held at a constant length for a specific duration of time to allow the complete system to settle and achieve a new static equilibrium state. The application of artificial forces and moments to the excavator system is intended to minimize the duration of time required for the system to settle, in turn reducing the computational burden involved in calculating the static conditions for the excavator system.

To optimize the effectiveness of the artificial forces and moments, f_T is gradually increased from 0 to 1, and vice versa. During the time period when the hoist or drag ropes are reeling in or paying out, f_T is small to allow the system to maneuver without impedance from artificial loads. The upper limit on all artificial force and moment factors (f_{TV} and f_{RV}) also allows the system to maneuver when the velocity is relatively high while at the same time preventing artificial loads from destabilizing the system. The lower limit on all the artificial force and moment factors (f_{TV} and f_{RV}) is necessary to increase the artificial forces and moments when velocity is low so that settling time is minimized. Without a lower limit on f_{TV} and f_{RV} , the velocity of the system elements after a move is small but not negligible, resulting in relatively small artificial forces. The lower limit on f_{TV} and f_{RV} eliminates these minor vibrations very quickly.

EXAMPLE RESULTS

In order to illustrate the utility of this numerical technique, consider an exemplar 1/16th scale dragline excavation system with physical properties delineated in Tables 1 and 2 and artificial force characteristics given in Table 3. In the example simulation shown, five different equilibrium positions are achieved by intermittently changing the length of the drag rope while holding the hoist rope length fixed. The drag rope and hoist rope are initially set to 15.1 ft and 26.25 ft, respectively. At $t = 0$ sec, the drag rope length is decreased by 1/2 ft in one second, while the hoist rope length is unchanged. The system then settles for ten seconds. Then, the drag rope length is again decreased by 1/2 ft in one second. This process is repeated for five different

drag rope lengths: 15.1 ft, 14.6 ft, 14.1 ft, 13.6 ft, 13.1 ft. For the entire event, the excavator boom azimuth angle equals zero. Figures 6–8 show the time history of the position of the mass center of the bucket and the pitch angle of the bucket for the conditions above. Two cases are shown. The solid line is the response of the system with artificial forces and moments as discussed previously while the dashed line presents the response of the same system without artificial forces and moments. Initially, at $t = -19$ sec, all rope segments are slightly slack. The system quickly settles to a steady state using artificial forces and moments. This steady-state condition is used to begin the case where no artificial force and moments are incorporated. Notice that the response with artificial forces and moments settles to a new static condition within a few seconds while the response without artificial forces and moments does not settle within 10 seconds. With the hoist rope length set to 26.25 ft and the drag rope length of 15.1 ft, the bucket pitch angle is about -65° (Figure 8). As the drag rope length is discretely decreased the bucket carry angle steadily increases to approximately -50° , -34° , -17° , -3° . Also, as the drag rope length is incrementally decreased the bucket incrementally moves closer to the boom. The discrete changes in drag rope length cause changes in the static conditions in the longitudinal plane, thus, the lateral component of motion is caused only by the nonsymmetric mass properties of the system and is small.

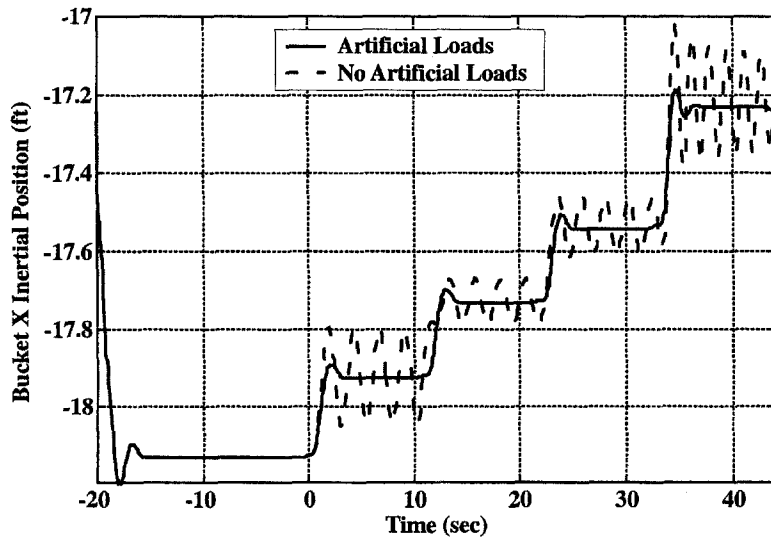


Figure 6. X position of bucket vs. time with and without artificial forces.

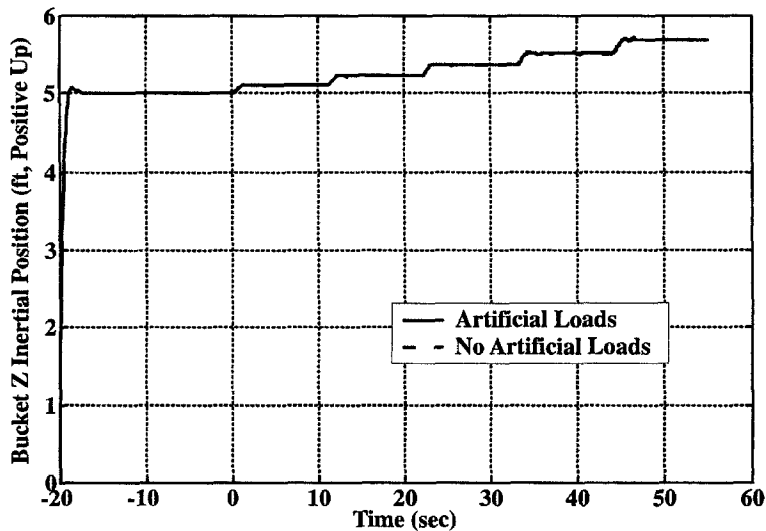


Figure 7. Z position of bucket vs. time with and without artificial forces.

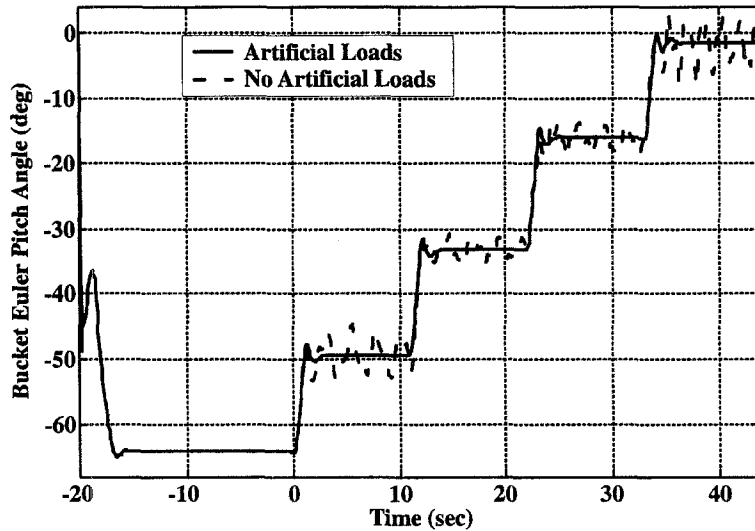


Figure 8. Pitch angle of bucket vs. time with and without artificial forces.

Table 1. Physical properties for rigid bodies.

| Parameter | Bucket | Drag Cluster | Hoist Cluster | Spreader Bar |
|---|---------|--------------|---------------|--------------|
| Mass, m_B (slug) | 0.3767 | 0.00623 | 0.0232 | 0.022600 |
| C.G. Location SL_B (ft) | 0.3058 | 0.0 | 0.0 | 0.0 |
| C.G. Location, BL_B (ft) | 0.0 | 0.0 | 0.0 | 0.0 |
| C.G. Location, WL_B (ft) | -0.0680 | 0.0 | 0.0 | 0.0 |
| Inertia, $I_{B_{XX}}$ (slug ft ²) | 0.05254 | 0.000005 | 0.000048 | 0.003401 |
| Inertia, $I_{B_{YY}}$ (slug ft ²) | 0.06333 | 0.000022 | 0.000545 | 0.000025 |
| Inertia, $I_{B_{ZZ}}$ (slug ft ²) | 0.00881 | 0.000018 | 0.000510 | 0.003390 |

For a given dragline rigging, a static pose chart of a dragline excavation system plots the position and carry angle of the bucket for a matrix of hoist rope and drag rope lengths. Initially, the hoist rope length is fixed while the drag rope is incremented through its range, followed by incrementing the hoist rope length once and repeating the drag rope increment. This is repeated until the hoist rope has been incremented through its entire range, creating a full matrix of the excavator bucket positions and carry angles.

Bucket pose for each cycle is determined both experimentally and using the simulation methodology described above. As shown in Figure 9, the scaled dragline excavator system is comprised of four rigid bodies; the bucket, spreader bar, hoist cluster, and drag cluster. Weights, inertial properties, and center of mass location for each body are listed in Table 1. The scaled dragline excavator system also employs three ropes (drag, dump, and hoist ropes), and six chains (left drag chain, left lower hoist chain, left upper hoist chain, right drag chain, right lower hoist chain, and right upper hoist chain). Both the drag and hoist lines are half inch rope, the dump line is quarter inch rope, and all chains are 3/8 in closed link chain. Chain and rope properties are listed in Table 2. The assembled bucket and rigging system weighs 24 lb f.

Position of each body and a portion of the drag and hoist ropes is tracked using a 3-D optical position analysis system from VICON Motion Systems [8]. Spherical reflective markers, 5 millimeter in diameter are placed on each body of interest. As shown in Figure 10, six cameras strategically placed throughout the laboratory emit and collect visible red light reflected from the markers. Using optical correlation techniques the position of the center of each marker is determined in three dimensions. This data is time stamped and stored in a text file which is then used to determine drag and hoist rope lengths along with body position and orientation.

Table 2. Physical properties for rope segments.

| Rope Segment | Number of Particles | Rope Mass (slug/ft) | Total Rope Length (ft) |
|-------------------------|---------------------|---------------------|------------------------|
| Drag Rope | 6 | 0.00141 | 10.0 |
| Dump Rope | 5 | 0.00152 | 3.57 |
| Hoist Rope | 10 | 0.00141 | 20.0 |
| Left Drag Chain | 5 | 0.01165 | 1.9375 |
| Left Lower Hoist Chain | 2 | 0.01165 | 0.5625 |
| Left Upper Hoist Chain | 3 | 0.01165 | 0.9167 |
| Right Drag Chain | 5 | 0.01165 | 1.9375 |
| Right Lower Hoist Chain | 2 | 0.01165 | 0.5625 |
| Right Upper Hoist Chain | 3 | 0.01165 | 0.9167 |

Table 3. Artificial force and moment properties.

| System Component | Artificial Force Factor | Artificial Moment Factor | Maximum Artificial Force (lb) | Minimum Artificial Force (lb) | Maximum Artificial Moment (ft*lb) | Minimum Artificial Moment (ft*lb) |
|-------------------------|-------------------------|--------------------------|-------------------------------|-------------------------------|-----------------------------------|-----------------------------------|
| Drag Rope | 0.252 | N/A | 176.4 | 0.0003 | N/A | N/A |
| Dump Rope | 0.079 | N/A | 53.9 | 0.0001 | N/A | N/A |
| Hoist Rope | 0.266 | N/A | 181.3 | 0.0003 | N/A | N/A |
| Left Drag Chain | 0.4032 | N/A | 274.4 | 0.0004 | N/A | N/A |
| Right Upper Hoist Chain | 0.259 | N/A | 176.4 | 0.0003 | N/A | N/A |
| Left Upper Hoist Chain | 0.259 | N/A | 176.4 | 0.0003 | N/A | N/A |
| Right Drag Chain | 0.403 | N/A | 274.4 | 0.0004 | N/A | N/A |
| Right Lower Hoist Chain | 0.238 | N/A | 161.7 | 0.0002 | N/A | N/A |
| Left Lower Hoist Chain | 0.238 | N/A | 161.7 | 0.0002 | N/A | N/A |
| Bucket | 0.049 | 0.9559 | 308.89 | 0.0377 | 1,329.9 | 0.000 |
| Spreader Bar | 0.0029 | 0.0523 | 18.53 | 0.0023 | 72.7 | 0.000 |
| Drag Cluster | 0.0001 | 0.0003 | 5.11 | 0.0006 | 0.5 | 0.000 |
| Hoist Cluster | 0.0031 | 0.0085 | 19.02 | 0.0023 | 11.8 | 0.000 |

For the example system mentioned above, Figure 11 displays the static pose charts for three hoist rope lengths. In Figure 11, the solid line and circles represent measured bucket pose while the dashed line and cross' represent predicted pose. For clarity, the bucket carry angle for Cycle I, Cycle II, and Cycle III is shown in Figures 12–14. Bucket position is predicted well for each cycle with a maximum difference of 3.2 inches. Predicted carry angle remains within 5° of measured values throughout the first two cycles. Cycle 3 bucket predicted carry angle remains within 8° of measured values.

Predicted bucket position in Cycle I matches measured values within 3.1 inches. Maximum differences occur between points 3 through 6 and 13 through 16 of 16. Cycle I bucket pitch angle follows a similar trend with a maximum difference of 5° occurring between points 3 through 6 and 13 through 16 of 16. Predicted bucket position in Cycle II matches measured values within 2.2 inches, maximum differences occur at points 2 through 5 and 11 of 11. Cycle II bucket pitch angle follows a similar trend with a maximum difference of 5° occurring at points 2 through 5 and 11 of 11. Predicted bucket position in Cycle III matches measured values within 3.2 inches, maximum differences occur at points 6 through 8 of 8. Cycle III bucket pitch angle remains

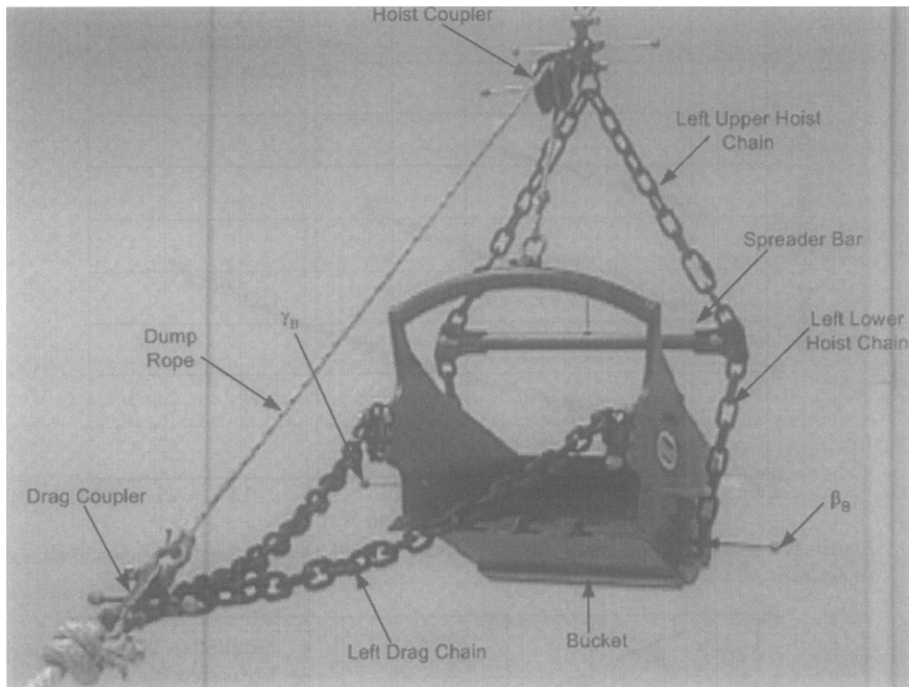


Figure 9. 16th scale dragline excavator rigging.

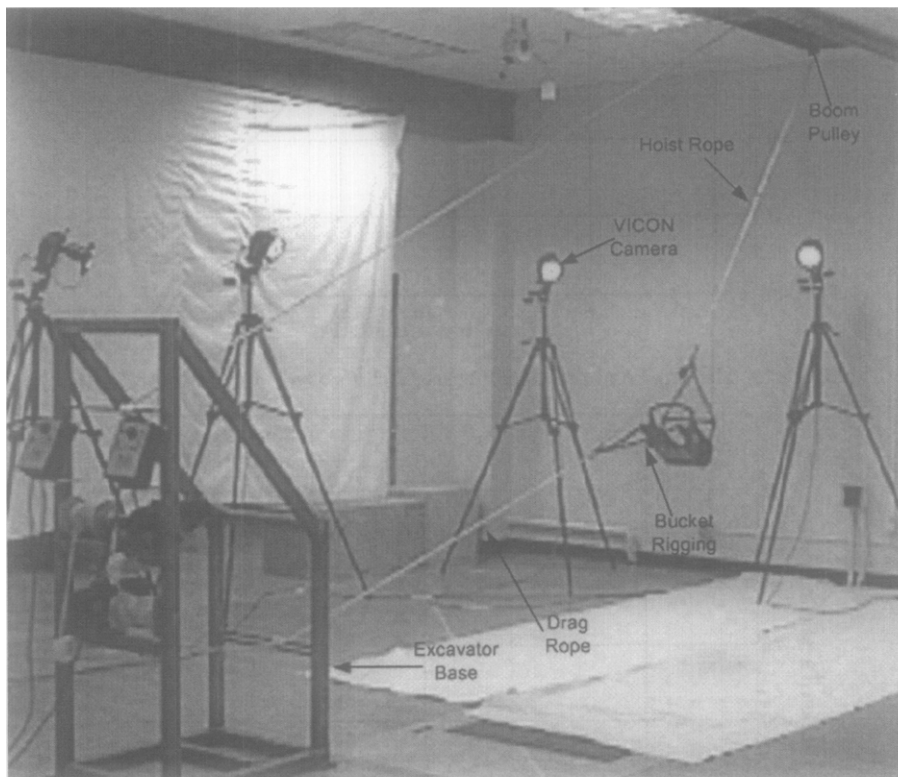


Figure 10. 16th scale dragline excavator system.

within 8° of measured values with maximum differences occurring between points 6 through 8 of 8.

Comparison results show in general when predicted and measured carry angle data match, bucket positions also match. Due to system rigging, the relationship between pitch angle and

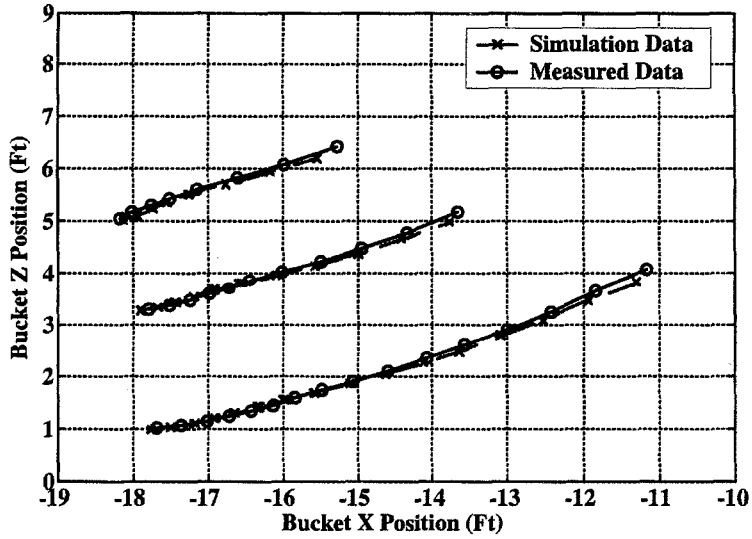


Figure 11. Measured and predicted static pose Cycle I (hoist rope 31 ft)—Cycle III (hoist rope 26.9 ft).

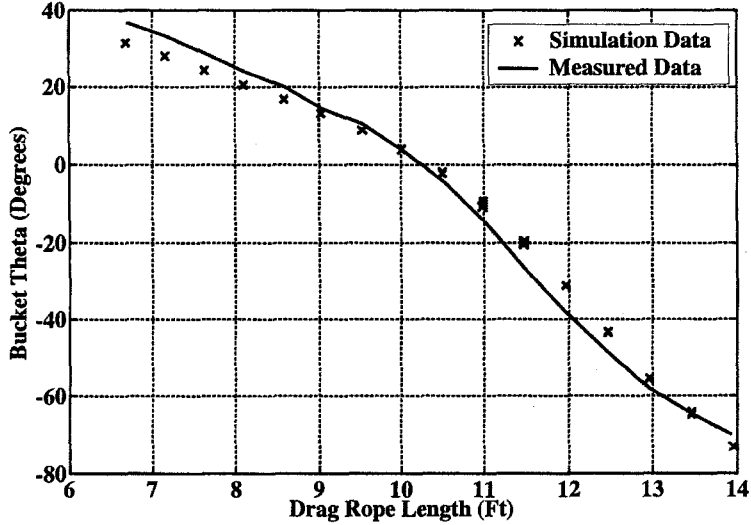


Figure 12. Measured and predicted bucket pitch for Cycle I (hoist rope 31 ft).

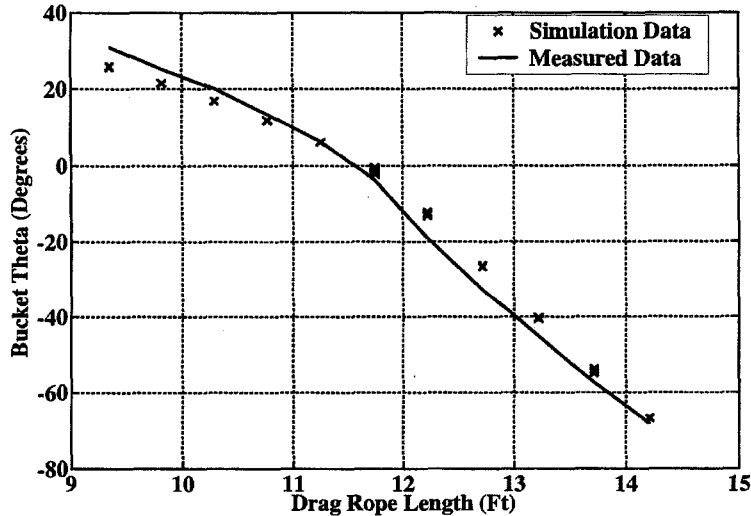


Figure 13. Measured and predicted bucket pitch for Cycle II (hoist rope 28.8 ft).

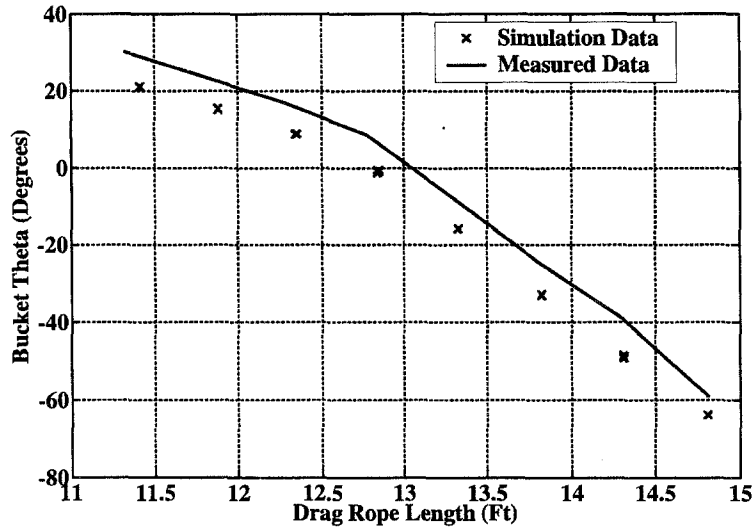


Figure 14. Measured and predicted bucket pitch for Cycle III (hoist rope 26.9 ft).

bucket mass center position are highly coupled. The simplified model used for the hoist cluster pulley seems to be a significant contributor to differences between measured and predicted data.

CONCLUSIONS

A method to rapidly generate static conditions for a complex three-dimensional dragline excavation system has been presented using dynamic simulation. The bucket, spreader bar, hoist cluster, and drag cluster are modeled as rigid bodies with 6 degrees of freedom apiece while the drag rope, hoist rope, dump rope, hoist chains, and drag chains are discretized into a finite number of point masses or beads that each allow 3 degrees of freedom. A specialized method to numerically obtain the static equilibrium state of a conventional dragline excavation system is developed where the dynamic equations of motion are integrated to a steady state with the drag rope and hoist rope lengths fixed. A novel aspect of the method is that artificial forces and moments are appended to the dynamic equations that dramatically improve convergence to a steady state while not changing the equilibrium condition. This method is exercised in generating static pose of an exemplar dragline excavation system. The numerically generated results agree well with experimental measurements on a 16th scale dragline excavator system.

REFERENCES

1. C.E. McCoy and J.L. Crowgey, Anti-tightline control system for draglines used in the surface mining industry, CH1575-0/80/0000-0140, *IEEE*, (1980).
2. D.K. Haneman, H. Hayes and G.I. Lumley, Dragline performance evaluations for tarong coal using physical modeling, In *Third Large Open Pit Mining Conference*, Mackay, August 30–September 3, (1992).
3. K. Pathak, K. Dasgupta and A. Chattopadhyay, Determination of the working zone of a dragline bucket, *Mining Technology*, (February 1992).
4. D.W. Hainsworth, P.I. Corke and G.J. Winstanley, Location of dragline bucket in space using machine vision techniques, In *Fifth Large Open Pit Mining Conference*, (1994).
5. P. Ridley and P. Corke, Calculation of dragline bucket pose under gravity loading, *Mechanism and Machine Theory* **35**, 1431–1444, (2000).
6. W.H. Press, S.A. Teukolsky, W.T. Vetterling and B.P. Flannery, *Numerical Recipes*, ISBN 0-521-43064-X, Cambridge University Press, New York, NY, (1992).
7. J.H. Ginsberg, *Advanced Engineering Dynamics*, pp. 119–162, Cambridge University Press, New York, NY, (1995).
8. VICON Motion Systems Limited, *Vicon System Manual*, 12th Edition, Vicon 612, (July 2002).